JOURNAL OF SPACECRAFT AND ROCKETS
Vol. 34, No. 6, November–December 1997

Galileo Probe Heat Shield Ablation Experiment

Frank S. Milos*
NASA Ames Research Center, Moffett Field, California 94035-1000

The Galileo Probe deceleration module contained an experiment that measured the surface recession of the forebody heat shield during the hypersonic entry into the Jovian atmosphere. A detailed description of the experiment, reduction of the recession data, reconstruction of the heat-shield shape history, and comparisons with preflight predictions are presented. Sensor performance was compromised by an extraneous signal during the first half of the hypersonic entry, but data quality was reasonably good for the second half of the entry. To within measurement accuracy the ablation was axisymmetric, and the final shape was well defined. Stagnation point recession was significantly less than predicted. Frustum recession exceeded predictions and was comparable to stagnation point recession.

Nomenclature

A = base area, cm^2
C_D = drag coefficient
c = curve fit constant, s^{-1}
d = base diameter, cm
g_e = Earth standard gravity, 9.81 m/s^2
l = recession lower bound, cm
M = total probe mass, kg
m = forebody heat shield mass, kg
R = radius, cm
r = radial coordinate, cm
S = streamlength from nose, cm
s = recession, cm
t = time after entry, s
t_m = time of maximum recession rate, s
u = recession upper bound, cm
z = axial coordinate, cm
Δs = recession uncertainty, cm
Δt = time uncertainty, s
θ = polar coordinate, deg

Subscripts

B = base
i = index for six S/R_N locations
N = nose

Introduction

THE Galileo Probe deceleration module encountered the most severe heating environment ever experienced by a planetary entry probe when it entered the atmosphere of Jupiter at a relative velocity 47.4 km/s on Dec. 7, 1995. As the probe decelerated from Mach 50, the forebody heat shield had to survive peak heating rate and heat load on the order of 30 kW/cm^2 and 300 kJ/cm^2, respectively, and deceleration of 250 g_e for nominal entry conditions.[1–4] The heat shield also had to maintain the structural bondline temperature below 644 K prior to parachute deployment, which released the heat shield from the descent module containing the primary scientific instruments.[1,3]

Figure 1 shows a cross section of the deceleration module.[5,6] The forebody exterior shape was an axisymmetric sphere-cone with 22.2-cm nose radius and 44.86-deg half-angle. The nosecap was chopped-molded carbon phenolic, the frustum was tape-wrapped carbon phenolic, and the aft heat shield was phenolic nylon. The forebody heat shield thickness decreased from 14.6 cm at the centerline to a minimum of 5.1 cm at the front of the frustum, then increased to 5.4 cm at the rear of the frustum. This thickness distribution provided a 50% safety margin against conservative predictions of heat shield recession for the nominal axisymmetric entry at −8.6 deg into a nominal atmosphere containing 89% H_2 and 11% He.[3] This margin was believed to be adequate for probable survival of the probe under a worst-case scenario of steep entry at −10.0 deg into a cool-heavy atmosphere containing 25% He. As summarized in Table 1, the actual entry was slightly shallow (−8.4 deg),[7] and the atmosphere was somewhat heavy (13.6% He).[8,9] The probe survived this entry as expected.

One scientific objective of the mission was to determine the temperature, pressure, and density profiles of the Jovian atmosphere. The descent module contained an atmospheric structure instrument,[10] which directly measured the relevant quantities for this atmospheric reconstruction during the parachuted descent of the probe following heat shield separation. During the deceleration period, however, the atmospheric structure must be indirectly calculated from measured decelerations and knowledge of the atmospheric composition, the probe trajectory, variation of C_D along the trajectory, and probe mass and diameter histories. The shape-related quantities could only be obtained by direct measurement of the heat shield recession; thus, a heat shield ablation experiment was created to provide this information. The General Electric Re-Entry Systems Division was commissioned to design, build, and install the experiment with the following requirements.[11]

1) The total mass loss and forward heat shield recession shall be deducible throughout the high-speed entry based on measurement and analysis such that the ratio of probe mass to frontal cross-sectional area is known to within ±2.6% (including data handling uncertainties).

2) The final configuration after ablation shall be known with sufficient accuracy to allow determination of the drag coefficient to within ±5%.

3) A total of 10 sensors shall be used: two near the stagnation point, two on the edge of the heat shield, and six at intermediate points selected to best define the heat shield mass and shape change.

4) Each sensor shall provide a measure of the local heat shield recession to within ±0.127 cm (excluding data handling uncertainties).

5) These requirements shall be met with a total of 912 data points.

The purpose of the present work is to document the heat shield ablation experiment, the data obtained from Jupiter, reduction of the probe data, reconstruction of the heat shield shape, and comparison of the heat shield performance with preflight predictions.

Heat Shield Ablation Experiment

Ten analog resistance ablation detector (ARAD) sensors were installed[12] in the forebody heat shield at six S/R_N locations as illustrated in Figs. 2 and 3. Sensors 1 and 2 were installed on the

Received July 25, 1996; revision received May 12, 1997; accepted for publication May 22, 1997.

*Aerospace Engineer, Thermal Protection Materials and Systems Branch, MS 234-1. Senior Member AIAA.

Table 1 Galileo probe entry conditions

	Nominal (range)	Actual
Entry velocity, km/s	47.8	47.4
Entry angle, deg	−8.6 (±1.4)	−8.4 ± 0.1
Attack angle, deg	0 (0–6)	<1.0
Mole percent He	11 (0–25)	13.6 ± 0.3
Molecular weight	2.22 (2.0–2.5)	2.35[a]
Rotation rate, rpm	10.5 ± 0.5	10.5

[a]Including heavy trace species NH_3 and CH_4 (Ref. 9).

Table 2 ARAD geometric information

ARAD	Initial ARAD tip location r	z	θ	S/R_N	Initial length, cm
1	8.30	1.61	90	0.38	14.40
2	8.30	1.61	270	0.38	14.30
3	22.00	12.83	31.5	1.19	7.75
4	31.77	22.73	42.5	1.81	5.48
5	43.43	34.45	128	2.55	5.40
6	43.43	34.45	232.0	2.55	5.38
7	54.97	46.04	325.50	3.28	5.53
8	54.97	46.04	55.00	3.28	5.58
9	63.25	57.61	47.25	3.96	5.50
10	63.25	57.61	192.75	3.96	5.59

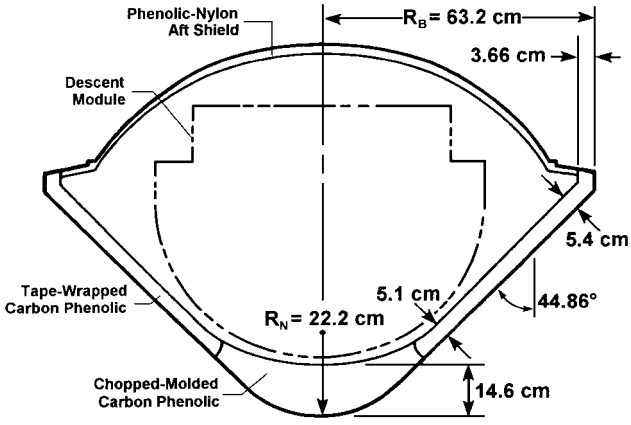

Fig. 1 Cross section of Galileo Probe deceleration module.

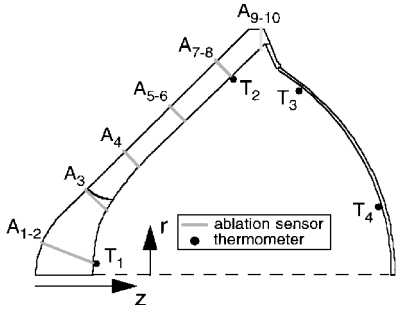

Fig. 2 Illustrated locations of 10 ablation sensors (A_1–A_{10}) in heat shield and four resistance thermometers (T_1–T_4) inside structure; sensors are not coplanar.

spherical nose, six sensors (3–8) were distributed at intermediate points selected to define the frustum shape, and two sensors (9 and 10) were located on the cylindrical base to measure the radius. The circumferential distribution (Fig. 3) provided an indication of recession asymmetry, which was expected to be minimal for the nominal axisymmetric entry. Table 2 lists the initial ARAD locations and lengths. The tips of frustum ARADs 4–8 are colinear, but the tip of ARAD 3 is slightly offset owing to the presence of a small (0.08-cm) backward-facing step at the bondline between the nosecap and frustum heat shields.[13] To avoid ambiguity in defining the streamlength change at the bondline mismatch, the S/R_N locations in Table 2 were calculated by ignoring the existence of the backward-facing step.

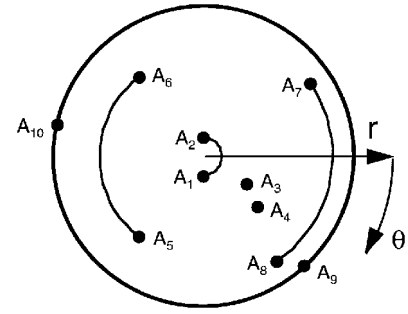

Fig. 3 Radial and circumferential distribution of ARAD sensors; view toward +z direction.

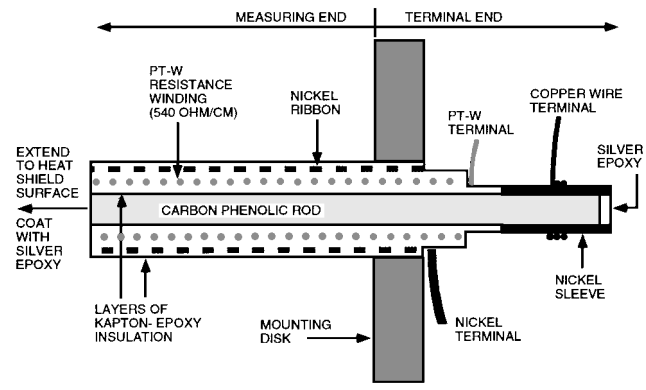

Fig. 4 ARAD.

Figure 2 also shows the locations of four resistance thermometers, which were bonded inside the aluminum structure of the deceleration module.[3,12] The thermometers showed a small, gradual increase in temperature starting after the end of ablation,[7] which is consistent with fact that in this severe entry environment ablation and pyrolysis dissipate most of the energy imparted to the heat shield. An analysis of the temperature data in relation to the heating environment and the measured ablation response is presented in Ref. 14. The fore and aft heat shields successfully protected the structure, despite the fact that parachute deployment and aeroshell separation occurred about 53 s late owing to miswiring of acceleration switches in the probe.[7,15]

An ARAD sensor[16] is a three-terminal electrical device that produces a voltage proportional to the length of the sensor. As shown in Fig. 4, the sensor contains three coaxial electrically conductive components: an inner carbon-phenolic rod, a closely wound helical coil of platinum tungsten wire, and a outer winding of nickel ribbon. The carbon phenolic rod and nickel ribbon have relatively low resistance, whereas the platinum tungsten wire is wound to a nominal resistance of 540 Ω/cm of ARAD length. Kapton® tape and epoxy are used to insulate the conductive elements. The ARAD sensor has a diameter of about 0.1 cm and can be wound to any desired length.

If the sensor tip is heated to sufficiently high temperature (above 800–900 K), the Kapton and epoxy layers pyrolyze to form a tenacious, conductive char that completes a circuit for electric current to pass through the ARAD. Because the ARAD is open circuited without a char layer at the tip, a coating of silver epoxy was placed on the outboard end of the ARADs to obtain preflight measurements of the sensor resistances. The coating had a tendency to peel off; therefore, the silver epoxy was occasionally reapplied for ground testing.[4] The initial ARAD lengths and resistances were used to define calibration constants for data reduction.[17]

After the forebody heat shield was bonded to the structure, holes for ARADs were drilled with surface-normal orientation from the outside, then countersunk through the structure so that the mounting disks could be approximately flush mounted to the inside surface of the heat shield.[11,18] The ARADs were bonded with epoxy to the heat shield, wired appropriately, and potted to the structure. Owing to space limitations, ARADs 9 and 10 were not flush mounted but instead protruded inside the structure near the base and were potted to the frustum structure.[12]

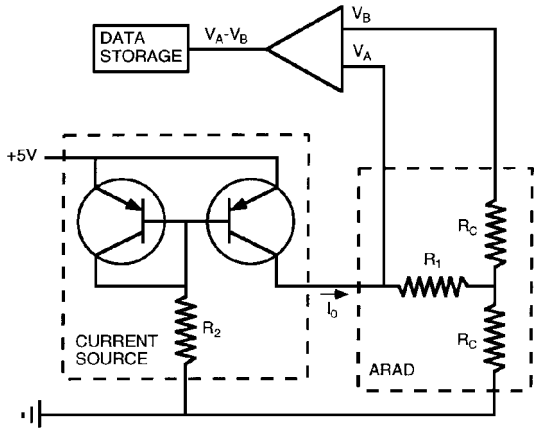

Fig. 5 ARAD circuit diagram.

A diagram of the ARAD circuit[19,20] is presented in Fig. 5. The sensor is driven by a precision constant-current supply consisting of a matched pair of transistors and a current-determining resistor R_2. The current through R_1 remains relatively constant, depending on the characteristics of the transistors, while the voltage V_A decreases as the sensor shortens during ablation. Because the voltage V_A is also determined by the char resistance R_C, another voltage V_B is required to indicate the effect of char resistance. The difference between the voltages V_A and V_B becomes a measure of the sensor resistance R_1, which is proportional to the uncharred length of ARAD. In operation, the heat shield and embedded ARAD ablate concurrently, and the uncharred ARAD length is a direct measurement of the heat shield thickness. The resistance of the sensor is $R_1 = (V_A - V_B)/I_0$, where I_0 is the source current. The current-source resistance is selected to provide a current compatible with a maximum char resistance of under 10 kΩ. A lower char resistance decreases the voltages V_A and V_B, but the difference $V_A - V_B$ is essentially independent of R_C. Precision current sources of 0.61 and 1.61 mA were used to drive ARADs 1–3 and 4–10, respectively.[21]

The sensors were described[3] as having a measurement error of ±0.091 cm. This value is consistent with the results of arc-jet testing of ARADs in the Giant Planet Facility,[22] which showed ARAD data accurately measuring recession up to a maximum recession rate of 0.1 cm/s. The final ARAD recession was within 0.06 cm of posttest measurements. However, it should be noted that the maximum recession rate for the Galileo heat shield was about 0.4 cm/s, which is four times the highest rate achieved in the ground tests.

During probe entry into the Jovian atmosphere, 12 minor frames of data were stored in recycling memory.[21] Each minor frame contained seven samples of each ARAD length, four char resistance measurements, and a calibration measurement from each current source.[21] The total number of data points was $12 \times 76 = 912$ of which 840 were ARAD voltage-difference measurements. All data passed through A/D conversion and were stored as 8-bit binary numbers (0–255 in decimal count value).[17] The stored data spanned the ablation portion of the trajectory and contained 84 measurements from each ARAD at an average sampling interval of 0.57 s.

ARAD data acquisition could be terminated by several conditional and unconditional events, based on the status of acceleration switches and resets, which occurred between 74.8 and 85.1 s after the probe reached an altitude 450 km above the 1-bar pressure level, which is defined herein as time zero for entry. Owing to the unknown effects of switch miswirings in the probe, the absolute timing of the ablation data is not known with certainty. A timing reconstruction study suggests that data acquisition terminated at an unconditional event about 81 s after entry,[7,15] but comparison of the recession and trajectory data indicates that ARAD data acquisition must have ended at or near the first conditional event at 74.8 s. Therefore, this earlier timing is used in this work.

ARAD Data Reduction

Data from the heat shield ablation experiment were transmitted from the Galileo orbiter to Earth several times after probe entry on Dec. 7, 1995. Each transmission contained some ambiguous data, but by the third transmission a complete data set was assembled. Calibration constants[17] were used to convert the recorded count values back into dimensional quantities, such as lengths for the ARAD sensors. The current sources performed flawlessly throughout the mission and varied by only one decimal count during entry. The char voltages were in the expected range, usually under 1 V, which confirms that the current-source resistance was sufficiently high to provide a constant current to the ARADs.

The entire ARAD data set, in the form of decimal count vs sample number (1–84), is presented in Fig. 6. The data are sorted by the six S/R_N locations shown in Fig. 2 and listed in Table 2. The first, fourth, fifth, and sixth locations have data from two sensors. ARAD 4 did not return a useful signal until sample 48 late in the trajectory. Conversely, ARADs 6 and 7 stopped functioning after sample numbers 55 and 67, respectively. Sensor 7 partially reactivated late in the trajectory, but recorded an incorrect (higher) count value. For the locations with duplicate sensors, the sensor pairs show similar trends except for a few bad data points and pegged data.

Every sensor returned some pegged count values of 255. Signal pegging occurs if the ARAD is open circuited or if the measured voltage difference exceeds the range of A/D conversion (5.12 V).[21] Open circuiting occurs if the three conducting elements in the ARAD are not electrically connected at the outboard tip either by the initial silver epoxy coating or by the thin char layer that forms when the surface temperature exceeds 800–900 K. The char layer may occasionally be blown or sheared off the ARAD tip, in which case a new char layer must form before a meaningful voltage is measured. Pegged voltages can conceivably occur if the source current is too high (which did not occur), if the voltage measurement offset drifts upwards, if an inadvertent current or voltage enters the circuit, or in the case of ARADs 7 and 8, if the initial sensor length is slightly too high to produce an unpegged voltage at the nominal source current. Because data can be pegged by several phenomena unrelated to sensor length, the pegged data points are not useful for determining ARAD recession.

Signal Noise and Bias

During preflight testing, voltages from ARADs 7 and 8 were pegged as expected, and the other ARAD signals varied from −4 to +1 counts from their calibrated values.[21] These data translate into a length measurement bias of from 0.00 to −0.12 cm for ARADs 1–3 and from +0.02 to −0.09 cm for ARADs 4–10. During inflight testing, ARADs 2, 7, and 9 were clearly pegged, and the other ARAD signals varied from 0 to −5 counts from calibration, including ARAD 8, which was not pegged.[23] Thus, the silver epoxy probably had peeled off ARADs 2, 7, and 9, and the length bias had drifted from −0.06 to −0.30 cm for ARADs 1–3 and from 0.00 to −0.12 cm for ARADs 4–10.

Interpretation of the flight data in Fig. 6 is not straightforward owing to the obvious noise prior to about sample number 40, particularly for ARADs 5, 6, 9, and 10, and to the fact that it is impossible to know which sensors, if any, were not open circuited. Because ARADs 2, 7, and 9 could not regain a conductive coating prior to reaching a surface temperature of at least 800–900 K, these sensors should have remained pegged throughout the initial stages of entry. Nevertheless, ARADs 7 and 9 both measure voltage variations prior to sample 20, which must be an extraneous signal unrelated to the sensor length. Similar oscillations are seen to a greater extent by ARADs 5, 6, and 10 and to a lesser extent by ARADs 3, 4, and 8.

The data from ARADs 9 and 10 are replotted on an expanded scale in Fig. 7. The signals clearly are not random noise, but appear to be oscillating with the probe rotation rate of 10.5 rpm at entry, i.e., one full rotation every 5.71 s or 10 samples. Several signal peaks are truncated by A/D conversion. The count minima from ARAD 10 consistently lag similar minima from ARAD 9 by 4–5 samples (2.3–2.85 s), which is consistent with the 145.5-deg angular separation of these sensors (Table 2) and the spin of the probe in the counterclockwise ($-\theta$) direction in Fig. 3. The data from ARADs 5 and 6 show the same period of rotation in Fig. 6, but in this case the signal from ARAD 6 lags the signal from ARAD 5 by only 2 or 3

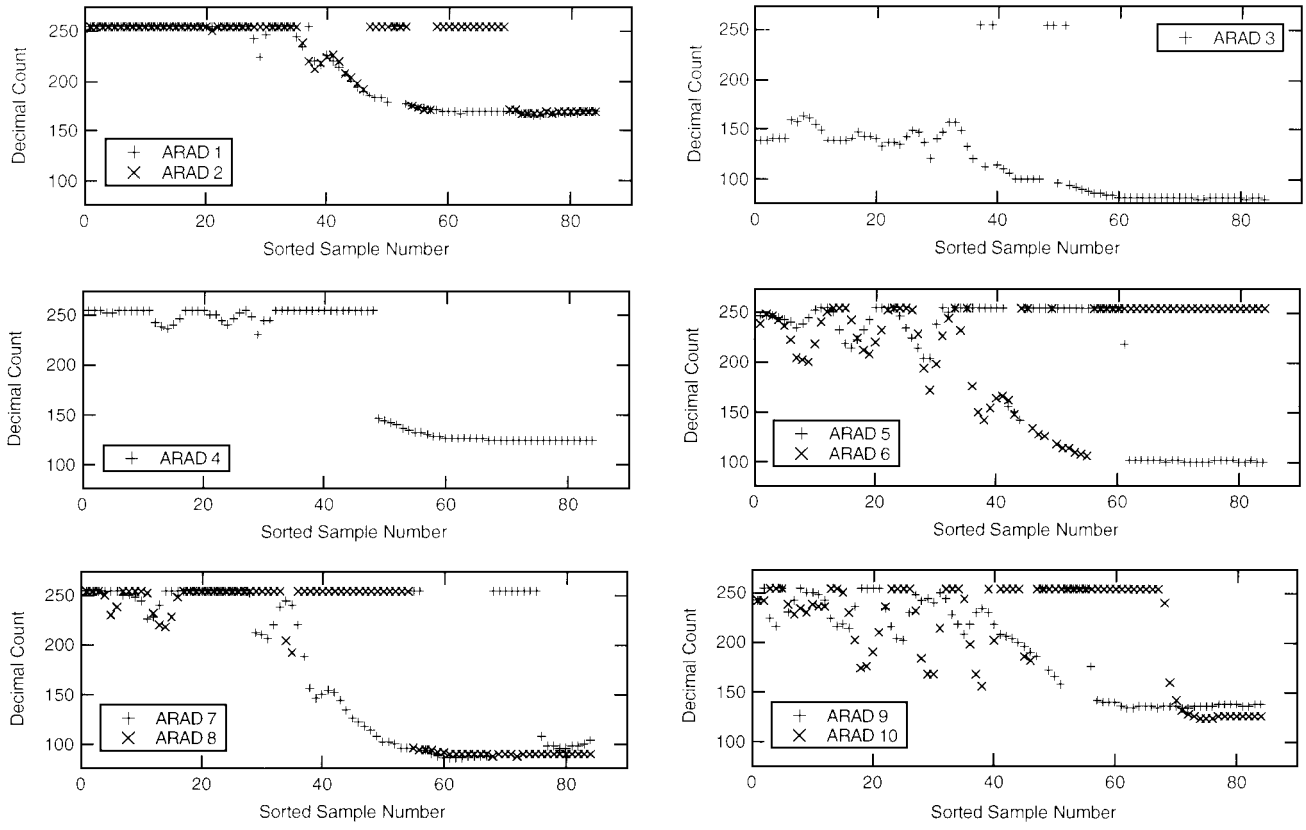

Fig. 6 ARAD data, sorted by S/R_N location.

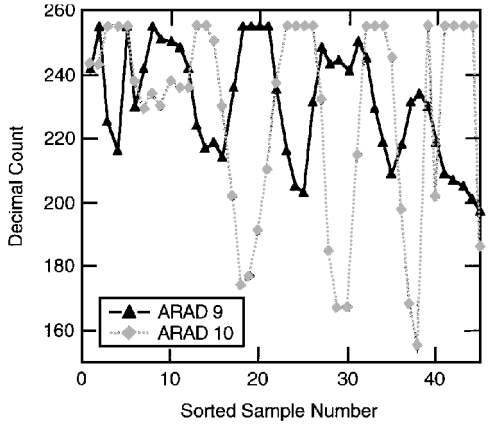

Fig. 7 Oscillations at 10.5 rpm in ARAD data; 10 samples in 5.7 s.

samples, which is consistent with the smaller 104-deg separation of these two sensors.

The author surmises that the probe surface acquired an electric charge or by some other mechanism interacted with ionized species in the high Mach number shock-layer plasma, which caused an inadvertent voltage signal in the ARAD circuit. This extraneous voltage oscillates around a nonzero mean value, and the oscillating part varies with θ position and time owing to the small angle of attack (about 1 deg) during entry. It is not clear why the various ARADs exhibit this phenomenon to different extents. However, the phenomenon subsides near sample number 40, perhaps owing to a combination of factors including the decrease in Mach number, the increase in pressure, and the massive surface blowing. A signal related to ARAD length emerges from the noise, and every sensor provides a well-defined postablation count value, except ARAD 6, which was approaching a steady value when it ceased functioning at sample number 56.

The question that arises is what offset bias should be applied to the ARAD length measurements? Unfortunately, no ARAD establishes a useful baseline count in the first half of the data. ARADs 5 and 6 and 9 and 10 are obviously corrupted by the extraneous signal. ARADs 2 and 7 were open circuited, and ARAD 8 cannot be used, because it must be pegged unless it still retained the silver epoxy coating and the length bias was worse than −2 counts. Only ARAD 3 is clearly not open circuited. This sensor has 11 of its first 20 measurements in the range 139.5 ± 1.5 counts, which superficially appears to establish a baseline 10 counts above the calibrated value of 129.3 counts. However, +10 counts would be a large offset in the opposite direction from the preflight and in-flight data. It is more likely that ARAD 3 is receiving the extraneous voltage in addition to the voltage proportional to its length, which causes the unrealistically high count values prior to sample number 40. Data from ARADs 1 and 4 could be similarly contaminated, and these sensors also may be open circuited.

Because the entry data do not establish a baseline for signal bias, the in-flight offset range from 0 to −5 counts is assumed for all ARAD measurements. Therefore, 2.5 counts are added to every ARAD data point prior to application of the calibration constant, and the total recession uncertainty is assumed to be the sum of nominal measurement uncertainty of ±0.091 cm plus the bias uncertainty of ±2.5 counts. This sum approximately equals ±0.25 cm for ARADs 1–3 and ±0.15 cm for ARADs 4–10.

Sensor Recession

The ARAD data from Fig. 6 are replotted in Fig. 8 as recession vs time from entry, sorted by S/R_N location. All pegged data and 14 other bad data points were excluded from the plots. The recession is obtained by adding the offset bias to the ARAD count value, multiplying by the calibration constant to obtain the sensor length, and then subtracting the computed length from the known initial sensor length. The recession uncertainty is shown in the upper left corner of each plot. Also plotted on Fig. 6 are curve fits and bounding curves, which will be described later. The same vertical scale is used on each plot to facilitate comparison of the data from different locations.

The large oscillations in the data prior to 50 s contradict the measurement uncertainty shown in the figures; however, as discussed earlier, these oscillations are believed to be caused by an extraneous voltage signal, not a sensor malfunction. The magnitude of the extraneous signal appears to decay near 50 s, data quality improves

to the point where a definite signal is observed, and the sensor pairs agree to within the nominal uncertainty shown on the figures. Unfortunately, at least 50% of the recession history is corrupted by the extraneous signal.

The good agreement between the pairs of duplicate sensors confirms the ablation was axisymmetric to measurement accuracy. ARADs 9 and 10 show the worst discrepancy, converging to final recession values of 2.50 and 2.66 cm, respectively. These values are within the estimated total uncertainty of ±0.15 for recession of ARADs 9 and 10. Axisymmetric average values for final recession at the six locations are listed in Table 3.

Probe Final Shape and Mass

Assuming axisymmetric ablation, the ARAD data or curve fits thereof provide six points on the heat shield surface at any time. The heat shield shape is reconstructed by defining a series of three conical frusta, which connect the four frustum points, defining a spherical nose that passes through the first point and is tangent to the extension of the first frustum section, extending the last frustum section toward the base, and truncating the geometry at a base radius given by the last ARAD point. Elliptical nose shapes are not precluded by the ARAD data, but the eccentricity is indeterminate given only one data point on the nose. Most preflight predictions show nonspherical ablated nosetips, because recession and heating are not constant over an entire spherical nosecap.[2,3,24,25] The drag coefficient varies with nose ellipticity, but the postablation value of C_D probably can be determined to within ±5% despite the uncertainty in nose shape.[26]

Figure 9 shows the reconstructed final ablated shape. The total recession is 4.45 ± 0.25 cm at the nose, decreasing to a minimum of 2.74 ± 0.15 cm at midfrustum, then increasing markedly to 4.00 ± 0.15 cm at the frustum near the base. More than 10 cm of heat shield remained at the nose, but only 1.40 ± 0.15 cm was not ablated at the end of the frustum. The most critical location for heat shield margin was after the end of the frustum on the small cylindrical base section where the final heat shield thickness was 1.08 ± 0.15 cm. The final forebody shape can be approximated by a sphere cone with 23.5-cm nose radius and 44-deg half-angle.

Using the final recession values and uncertainties from Table 3, the total forebody ablation is 79 ± 4 kg. To determine the final total probe mass, the mass losses from forebody pyrolysis and from aft heat shield ablation and pyrolysis must be taken into account. Transient charring material response calculations[25] for a lighter (310-kg)

Table 3 Axisymmetric final recession

ARAD	Final recession, cm	Heat shield thickness, cm	
		Initial	Final
1, 2	4.13 ± 0.25	14.15	10.02 ± 0.25
3	2.77 ± 0.25	7.40	4.63 ± 0.25
4	2.74 ± 0.15	5.17	2.43 ± 0.15
5, 6	3.13 ± 0.15	5.19	2.06 ± 0.15
7, 8	3.63 ± 0.15	5.30	1.67 ± 0.15
9, 10	2.58 ± 0.15	3.66[a]	1.08 ± 0.15[a]

[a]Relative to inside of heat shield base (cf. Fig. 2).

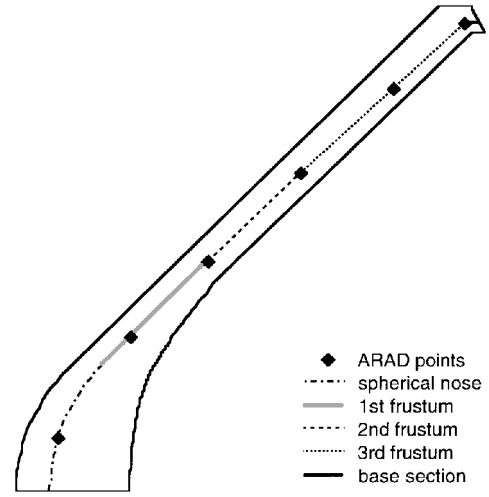

Fig. 9 Heat shield shape reconstruction.

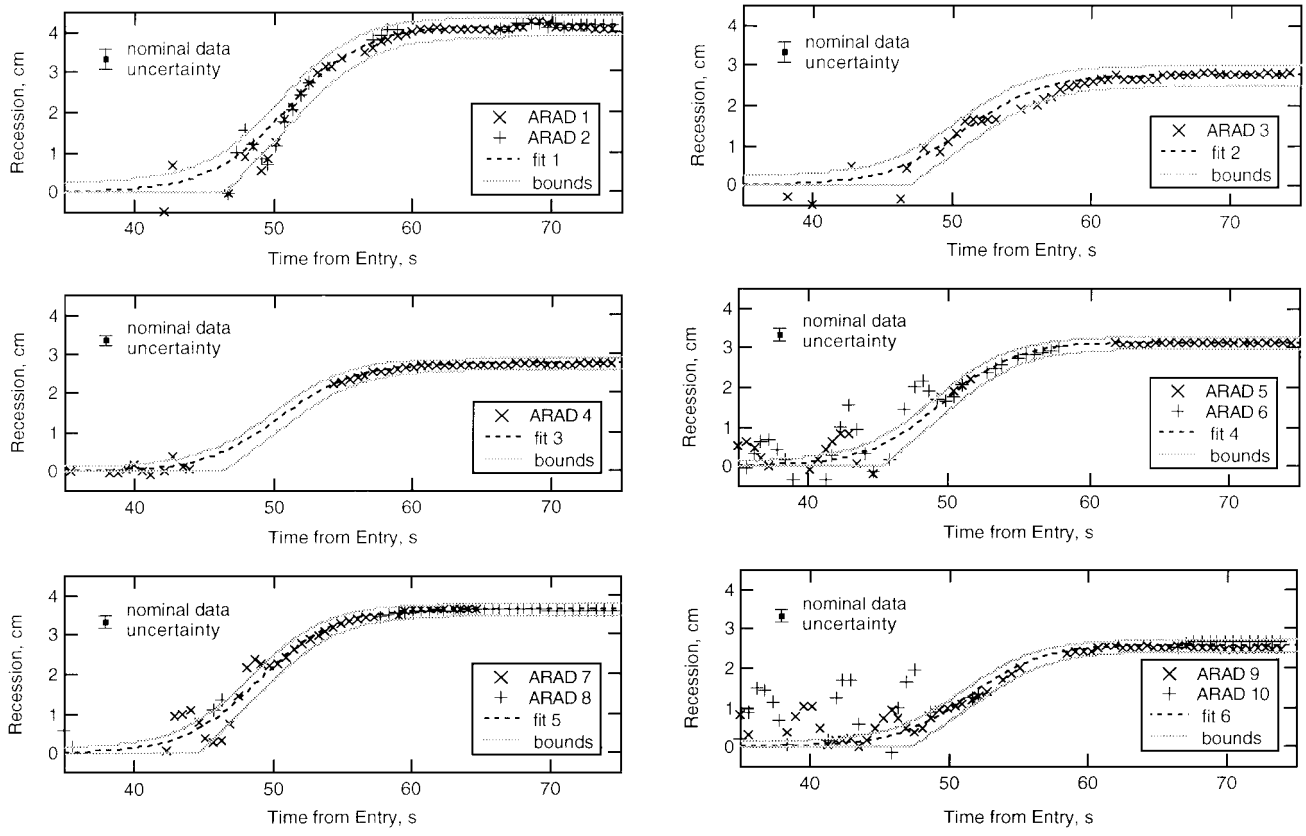

Fig. 8 ARAD recession and curve fits, sorted by S/R_N location.

Table 4 Probe mass properties

	Mass, kg
Entry mass	337
Less	
Forebody heat shield ablation	79.0 ± 4.0
Forebody heat shield pyrolysis	1.5 ± 0.5
Aft heat shield mass loss	8.4 ± 4.2
Final mass	248.1 ± 8.7

probe showed the equivalent of about 0.28 cm of fully charred material on the frustum. A straightforward calculation shows the final shape loses about 4 kg of mass per centimeter of char depth; thus, it is probably safe to estimate the final forebody pyrolysis mass loss as only 1–2 kg. The total aft mass loss was first estimated[3] at 6.9 kg and later increased[27] to 8.4 kg. These values were intended to be conservative but were assigned an uncertainty of ±50% owing to the difficulty of computing afterbody convective and radiative heating distributions.[28,29] As shown in Table 4, combination of the preceding estimates leads to a final probe mass of 248.1 ± 8.7 kg, which is a final mass uncertainty of ±3.5%.

From the data for ARADs 9 and 10 in Tables 2 and 3, the final diameter is 121.3 ± 0.3 cm. If the minimum diameter is associated with the minimum final mass, and the maximum diameter with the maximum final mass, the uncertainty in M/A at the end of ablation is at least ±3.0%, which slightly exceeds the ±2.6% requirement. The uncertainties in aft mass loss, ARAD measurement, measurement bias, and forebody pyrolysis account for approximately 48%, 27%, 19%, and 6% of the final M/A uncertainty, respectively.

Comparison with Predictions

Computations of heat shield requirements for the Galileo Probe considered a series of entry masses, which increased from under 300 kg in early studies up to 335 kg for the final probe design. Final preflight predictions using the design shape and mass were obtained from two codes. COLTS,[30] a viscous shock-layer code developed at NASA Langley Research Center, provided computational fluid dynamics (CFD) predictions of heat shield recession.[2] The thermodynamic outer planets insulation code (TOPIC)[31] was the primary design tool used by the General Electric Re-Entry Systems Division to predict heat shield recession.[3] TOPIC was an engineering code that combined computations and correlations of CFD and experimental data for shock shape, pressure distribution, carbon ablation thermochemistry, convective and radiative heat transfer and blockage, spallation, and other factors.

Figure 10 compares the recession obtained from the ARAD data with predicted final recession distributions[2,3] for the nominal entry and atmosphere. The two predictions from Ref. 3 used a nonreflecting surface, whereas the prediction from Ref. 2 (the dashed line) used a less conservative assumption of 10% surface reflectance. The COLTS predictions assumed turbulent flow on the nose at all times during entry, whereas TOPIC assumed abrupt transition to fully turbulent flow at a boundary-layer edge Reynolds number of 10^5. TOPIC predicted the greatest stagnation point recession despite the fact it used laminar flow correlations at the nose.

All predictions overestimated recession at the nose and underestimated recession over most of the frustum. The TOPIC design prediction shows recession of 8.75 cm at the nose, which is 96% high, and 3.27 cm at the end of the frustum, which is 18% low. The less conservative COLTS calculation shows 5.84 cm at the nose (31% high) and 2.29 cm at the end of the frustum (43% low). The ratio of frustum end to nosetip recession was less than 0.4 in these two calculations, but the measured ratio was 0.9.

Differences between the preflight and actual trajectory and atmospheric structure are two potential sources for the large discrepancy between predicted and measured recession. The actual trajectory and atmospheric data are listed in Table 5. The nominal trajectory was reasonably accurate as shown in Fig. 11. However, there are significant differences between the nominal atmospheric model and the reconstructed atmosphere in the altitude range of interest. Figure 12 compares the pressure, density, and temperature profiles of the Orton II nominal model (circa 1979) with the reconstructed atmospheric

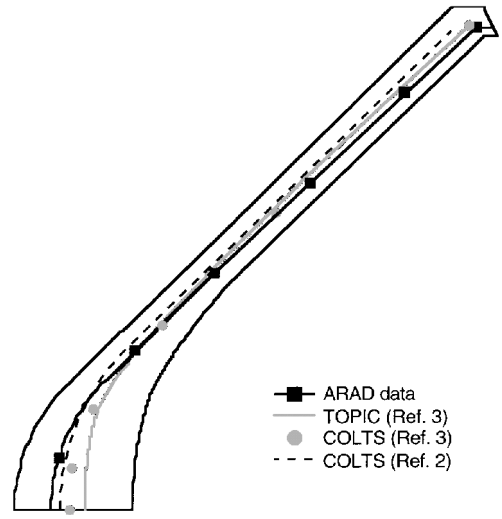

Fig. 10 Comparison of final shape with preflight predictions.

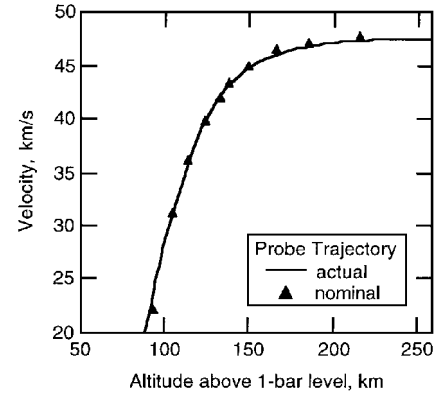

Fig. 11 Preflight nominal and actual entry trajectories.

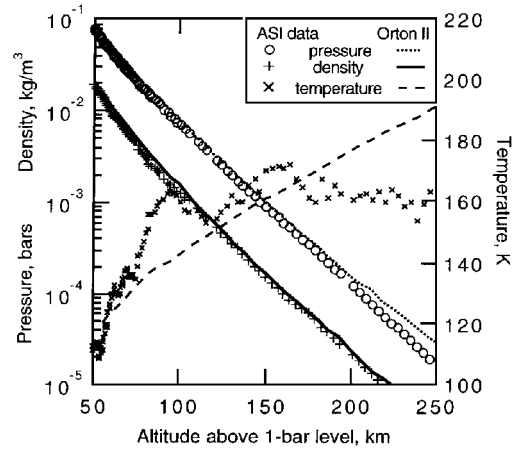

Fig. 12 Preflight nominal and reconstructed atmospheric structures.

data.[32] The pressure and density data match very well for altitudes from 50 to 200 km, but the temperature reconstruction deviates from the model by up to 21 K between altitudes of 90 and 190 km where 95% of the ablation occurs. More significantly, the measured[8,9] helium mole fraction of 0.136 is 24% higher the nominal value. The effect of increasing helium mole fraction is to increase shock-layer temperature and, consequently, to increase heating and ablation. The results in Refs. 24 and 25 show a 20–25% increase in peak heating rate for such an increase in helium mole fraction. If the recession predictions are increased 20% to account for the change in helium mole fraction, the predictions from Ref. 3 become close to the measurements at the rear of the frustum but even further in error at the nose.

Table 5 Entry trajectory and reconstructed atmosphere

Time, s	Altitude, km	Velocity, km/s	Density, kg/m^3	Pressure, bars	Temperature, K
0.00	450	47.406	3.47E-09	7.21E-08	527.8
7.30	400	47.429	9.92E-09	1.45E-07	381.9
14.80	350	47.451	5.65E-08	4.35E-07	210.8
22.50	300	47.468	3.05E-07	2.13E-06	195.9
30.44	250	47.446	2.77E-06	1.60E-05	163.2
34.51	225	47.368	7.73E-06	4.45E-05	162.8
38.67	200	47.135	2.16E-05	1.23E-04	160.4
40.35	190	46.951	3.16E-05	1.84E-04	165.0
42.06	180	46.674	4.81E-05	2.75E-04	161.9
43.79	170	46.256	7.03E-05	4.12E-04	165.8
45.55	160	45.667	1.00E-04	6.06E-04	170.6
47.36	150	44.813	1.49E-04	8.90E-04	168.9
49.21	140	43.531	2.27E-04	1.32E-03	164.3
51.16	130	41.591	3.49E-04	1.99E-03	160.8
53.23	120	38.617	5.56E-04	3.02E-03	153.6
55.52	110	34.296	8.34E-04	4.62E-03	156.6
58.19	100	28.440	1.23E-03	7.00E-03	160.6
61.57	90	21.342	1.85E-03	1.05E-02	160.1
66.35	80	13.544	3.06E-03	1.60E-02	147.8
74.55	70	6.352	5.30E-03	2.57E-02	136.9
89.77	60	2.261	9.48E-03	4.23E-02	126.3
111.02	50	0.833	1.89E-02	7.51E-02	112.4

The large discrepancy in the recession distribution warrants a reevaluation of the flowfield and radiation physics used in the CFD analysis. More than one aspect of the modeling may require modification to decrease nosetip heating without also decreasing the frustum heating. Nosetip recession predictions can be significantly reduced only by decreasing the absorbed radiative heat flux. This reduction can be accomplished by increasing the surface reflectance, by modifying the radiation or turbulence models, or by any change that reduces the shock-layer thickness. Frustum heating is a complex function of both turbulence and radiation modeling, because the turbulence history along the body affects both species and temperature profiles in the shock layer.

Some of the heavier spalled particles from the nose region could impact the frustum[33] and cause an erosion mass loss. However, the total spallation was calculated[2] at only 6% of the forebody ablative mass loss using spallation correlations for Galileo heat shield materials.[34] Because only a small fraction of spalled particles could have trajectories that impact the frustum, erosion by particle impacts was probably not significant. Spalled particles can, however, affect downstream radiative transport by releasing gaseous carbon species into the high-temperature portion of the shock layer.[33] This phenomenon was not included in preflight predictions.

Transient Shape and Mass Analysis

Owing to the noise and oscillations in the ARAD data prior to 50 s, it is impossible to determine precise histories for shape-related quantities such as d, M, and M/A during the first half of recession. Therefore, the approach taken in this work is to define curve fits to the sorted recession data, which can be extrapolated backward in time to provide nominal histories for axisymmetric recession at six locations on the forebody heat shield. The forebody shape history is calculated using the shape reconstruction methodology described earlier (cf. Fig. 9), and nominal histories for shape-related quantities are derived from the shape history. Upper and lower bounds to the curve fits are also defined to provide estimates of the uncertainty for all derived quantities.

Least squares curve fits to the recession data for $t > 45$ s were obtained numerically and in some cases improved manually using a visual fit to the data. The recession was fit with simple hyperbolic tangent functions s_i of the form

$$2s_i/s_{mi} = 1 + \tanh[c_i(t - t_{mi})]$$

which asymptotically approach the correct final recession values s_{mi} and which have a maximum slope at time t_{mi} when $s_i = s_{mi}/2$. The recession history is not necessarily a symmetrical function of $t - t_{mi}$, but the data quality is inadequate to justify the use of more sophisticated (skewed) fitting functions that would contain additional constants. Upper bound functions u_i were defined by shifting the curve fits upward by the measurement uncertainty Δs_i and backward by a time uncertainty Δt; i.e.,

$$2u_i/s_{mi} = 1 + \tanh[c_i(t - t_{mi} + \Delta t)] + 2\Delta s_i/s_{mi}$$

Lower bounds functions l_i were defined by shifting the curve fits downward by Δs_i and forward by Δt; however, in this case the curves were extrapolated linearly backward in time to provide a more conservative lower bound,

$$2l_i/s_{mi} = \max\begin{Bmatrix} 0 \\ \min\begin{Bmatrix} 1 + c_i(t - t_{mi} - \Delta t) - 2\Delta s_i/s_{mi} \\ 1 + \tanh[c_i(t - t_{mi} - \Delta t)] - 2\Delta s_i/s_{mi} \end{Bmatrix} \end{Bmatrix}$$

The nominal curve fits and the upper and lower bounding functions are presented with the recession data in Fig. 8, and the curve fit parameters are listed in Table 6. Curve fit 3 to ARAD 4 is speculative but is based on the curve fits obtained for the other sensors. The fitting functions are within the nominal uncertainty of the data after the extraneous oscillations dampen between 45 and 50 s. A time uncertainty $\Delta t = 0.5$ s provides reasonable bounds for the data, as shown in Fig. 8. The bounding functions indicate that recession uncertainty reaches a maximum between 45 and 50 s, then decreases to the nominal measurement uncertainty for $t > 60$ s. The uncertainty is highest for the first two locations because ARADs 1–3 are the most sensitive to voltage bias.

Figure 13 illustrates the heat shield shape history obtained from the nominal curve fits. The initial and final cross sections are shown, as well as one shape every 2 s between 46 and 56 s. The general trend is for peak recession rate to occur sooner on the frustum than on the nosecap, as indicated by the decreasing values of t_{mi} in Table 6. This trend may be a consequence of turbulence, which affects both convective and radiative heating, being more severe on the frustum than on the nosecap. The base recession, however, lags the frustum recession by more than 2 s.

The atmospheric reconstruction task requires time histories and uncertainties for d, M, and M/A. Diameter information is computed

Table 6 Curve fit parameters

ARAD	i	c_i, s^{-1}	t_{mi}, s	s_{mi}, cm	Δs_i, cm
1, 2	1	0.18	51.0	4.13	0.25
3	2	0.18	51.0	2.77	0.25
4	3	0.19	50.5	2.74	0.15
5, 6	4	0.19	49.5	3.13	0.15
7, 8	5	0.19	49.0	3.63	0.15
9, 10	6	0.19	51.5	2.58	0.15

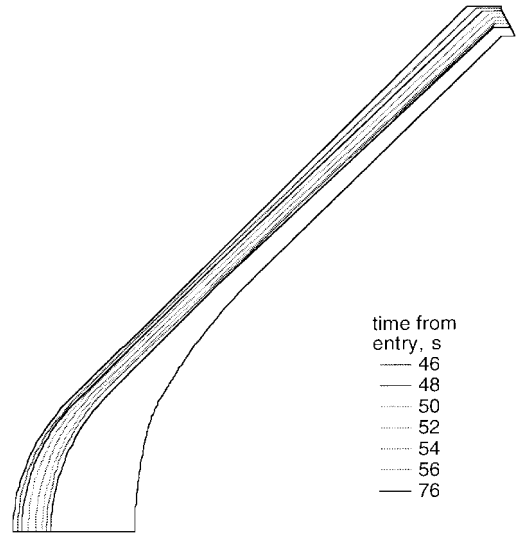

Fig. 13 Nominal heat shield shape history.

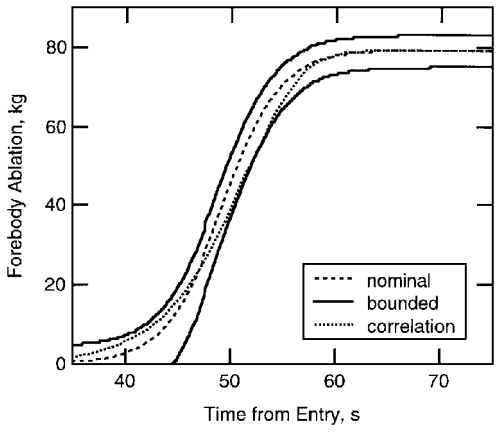

Fig. 14 Forebody ablative mass loss history.

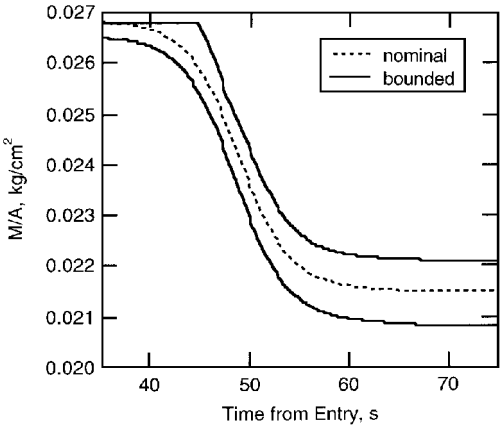

Fig. 15 Probe mass-to-area ratio history.

directly from the base recession curve fit and bounds, and the maximum diameter uncertainty is about 0.5%. The forebody ablative mass loss (Fig. 14) is calculated analytically from the shape histories obtained using the functions s_i, u_i, and l_i. The bounding curves in Fig. 14 differ by almost 18 kg at 45.25 s, but this difference decreases to 8 kg in the postablation regime. The nominal shape history produces a relatively symmetrical curve with a maximum ablation rate of 7.4 kg/s at 49.7 s. Figure 14 also shows an empirical mass loss correlation[26]

$$\Delta m = K \int \rho_\infty V_\infty^{6.9}\, \mathrm{d}t$$

derived from the COLTS solutions mentioned earlier, where the constant K was chosen to match the nominal mass loss of 79 kg. The correlation predicts a greater mass loss than the nominal curve at early time, but a lower maximum ablation rate of 6.2 kg/s at 51.6 s. It was noted earlier that the COLTS solutions did not predict the recession distribution accurately (cf. Fig. 10); nevertheless, the correlation lies within the uncertainty defined by the bounding curves.

The qualitative agreement of the correlation with the curve fits provides a validation of the recession data timing used in this work. Reference 7 suggests that the ARAD data and curve fits should be shifted 6.25 s later in time. This alternative timing, although not physically impossible, seems unlikely because 38% of the mass loss would occur after peak deceleration at 57.2 s.

The total probe mass is the entry mass minus the sum of the forebody ablation, the forebody pyrolysis, and the afterbody mass loss. Because the latter two quantities were unmeasured, the histories must be estimated. The afterbody mass loss and uncertainty from Table 4 were scaled proportionally with the forebody ablative mass loss. The forebody pyrolysis mass loss and uncertainty were increased linearly from zero at 50 s (near peak heating) to the Table 4 values at 70 s (postablation). Figure 15 shows the resulting M/A histories for the nominal and bounding shapes. The mass-to-area ratio decreases about 20% during the ablation portion of the trajectory.

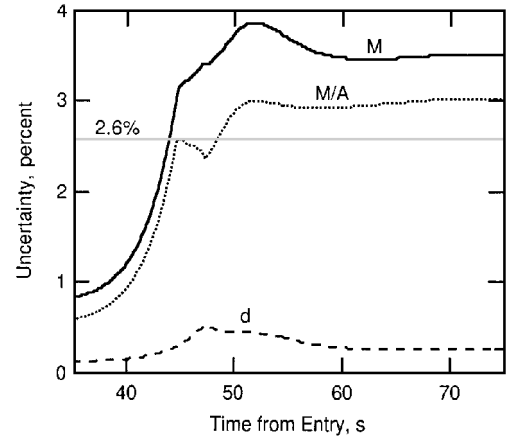

Fig. 16 Uncertainty histories.

The uncertainty in M, d, and M/A based on the bounding curves is presented in Fig. 16. If the minimum diameter is associated with the minimum mass and the maximum diameter with the maximum mass, M/A uncertainty is less than M uncertainty but nevertheless exceeds the $\pm 2.6\%$ requirement after peak heating. The uncertainty in M/A remains near $\pm 3\%$ for $t > 50$ s as the decreasing uncertainty in forebody ablation and base diameter is negated by the increasing uncertainty in the unmeasured mass losses from the aft heat shield and from forebody pyrolysis. As mentioned previously, the uncertainty in aft mass loss accounts for 48% of the final uncertainty in M/A. In hindsight, it would have been a good idea to obtain some direct measurements of the aft heating or recession, not only to reduce M/A uncertainty for the atmospheric reconstruction, but also to provide invaluable data for validation of afterbody heating models, which have high uncertainty in severe entry environments.

The preceding analyses do not take into account the pyrolysis mass loss that precedes ablation. Based on high-altitude heating results presented previously,[35] pyrolysis of the heat shield probably began before the probe reached an altitude of 300 km, which corresponds to an entry time of 22.5 s. However, the pyrolysis mass loss certainly was much less than 8.7 kg, which would be required for M/A uncertainty to exceed $\pm 2.6\%$ prior to the onset of ablation.

Conclusions

The Galileo heat shield ablation experiment has been described in detail. Embedded in the forebody heat shield were 10 ablation sensors, which were intended to measure recession to ± 0.127 cm and thereby enable determination of the probe mass-to-base-area ratio to $\pm 2.6\%$ during the hypersonic entry into the atmosphere of Jupiter. Data acquisition was successful, but sensor performance was compromised by an extraneous signal that introduced noise and oscillations into the first half of the data. This signal prevented establishment of a precise voltage baseline for the sensors, which increased the nominal measurement uncertainty to ± 0.25 cm on the nosecap and to ± 0.15 cm on the frustum. The magnitude of the extraneous signal decayed near the peak heating point in the trajectory, and the sensors provided the nominal accuracy for the second half of recession.

To within measurement accuracy the ablation was axisymmetric, and the final shape was well defined. Total recession was much less than predicted at the nose but exceeded predictions over most of the frustum. The most critical heat shield location was the end of the frustum at the base where about 1 cm of heat shield remained after ablation. The underprediction of frustum recession may be a direct consequence of the above-nominal helium mole fraction in the Jovian atmosphere, but explanation of the large overprediction of recession near the nose is more problematic.

The history and uncertainty of shape-related quantities was estimated by defining nominal and bounding curve fits to the recession data and by reconstructing the probe forebody shape history based on the curve fits. For lack of aft data, the unknown aft mass loss and its uncertainty were scaled with the forebody mass loss.

Probe total mass uncertainty varied from ±3 to ±4% after the onset of significant ablation. The total mass loss of 88.9 ± 8.7 kg was about half the initial heat shield mass. Probe mass-to-area ratio accuracy was not achieved after the onset of significant ablation. An uncertainty of at least ±3% for the final shape is attributable primarily to the uncertainty in the afterbody mass loss, which was not measured.

Acknowledgments

The author thanks R. A. Brewer, D. E. Carlock, and C. K. Sobeck for their assistance in obtaining reference information, locating design drawings, and processing the experimental data.

References

[1]"Galileo Probe System Critical Design Review, Book 1," Hughes Space and Communications Group, Hughes Aircraft Co., Rept. HS373-2275, Nov. 1981.

[2]Moss, J. N., and Simmonds, A. L., "Galileo Probe Forebody Flowfield Predictions," *Entry Vehicle Heating and Thermal Protection Systems: Space Shuttle, Solar Starprobe, Jupiter Galileo Probe*, edited by P. E. Bauer and H. E. Collicott, Vol. 85, Progress in Astronautics and Aeronautics, AIAA, New York, 1983, pp. 419–445.

[3]Talley, R. N., "Galileo Probe Deceleration Module Final Report," Re-Entry Systems Operations, General Electric Co., Rept. 84SDS2020, Jan. 1984.

[4]"Galileo Probe Final Project Report," Hughes Space and Communications Group, Hughes Aircraft Co., Rept. HS373-4500, Oct. 1990.

[5]"Heat Shield—Nose," Re-Entry Systems Operations, General Electric Co., Contract 08-737444-LD4, Drawing 47E526563, Philadelphia, PA, Aug. 1981.

[6]"Frustum Heatshield," Re-Entry Systems Operations, General Electric Co., Contract 08-737444-LD4, Drawing 47E523221, Philadelphia, PA, Aug. 1981.

[7]"Galileo Probe Mission Operations Final Report," Hughes Space and Communications Group, Rept. HS373-6000, Sept. 1996.

[8]Von Zahn, U., and Hunten, D. M., "The Helium Mass Fraction in Jupiter's Atmosphere," *Science*, Vol. 272, May 1996, pp. 849–851.

[9]Niemann, H. B., Atreya, S. K., Carignan, G. R., Donahue, T. M., Haberman, J. A., Harpold, D. N., Hartle, R. E., Hunten, D. M., Kasprzak, W. T., Mahaffy, P. R., Owen, T. C., Spencer, N. W., and Way, S. H., "The Galileo Probe Mass Spectrometer: Composition of Jupiter's Atmosphere," *Science*, Vol. 272, May 1996, pp. 846–849.

[10]Seiff, A., and Knight, T. C. D., "The Galileo Probe Atmosphere Structure Instrument," *Space Science Reviews*, Vol. 60, Nos. 1–4, 1992, pp. 203–232.

[11]"Galileo Probe Procurement Specification Deceleration Module," Hughes Space and Communications Co., Rept. PS32220-025, Rev. A, May 1981.

[12]"Sensor Installation—Aeroshell," Re-Entry Systems Operations, General Electric Co., Contract 08-737444-LD4, Drawing 47R523255, Rev. C, Philadelphia, PA, April 1982.

[13]"Shield Assembly Aeroshell," Re-Entry Systems Operations, General Electric Co., Contract 08-737444-LD4, Drawing 47E523222, Rev. A, Nov. 1981.

[14]Milos, F. S., "Analysis of Galileo Probe Temperature and Recession Data," AIAA Paper 97-2480, June 1997.

[15]"Calculation of Delay in Parachute Deployment Attributable to G-Switch Anomaly," Hughes Space and Communications Co., Rept. HS373-0020-3849, March 1996.

[16]"Analog Resistance Ablation Detector (ARAD)," Re-Entry Systems Operations, General Electric Co., Contract 08-737444-LD4, Drawing 47D523037, Rev. B, Philadelphia, PA, Aug. 1979.

[17]"Galileo Probe Telemetry Calibration Handbook," Space and Communications Group, Hughes Aircraft Co., Rept. SS32220-021, Rev. A, Jan. 1986.

[18]"ARAD/HILOK Drilling," Re-Entry Systems Operations, General Electric Co., Contract 08-737444-LD4, Drawing SK-777, Rev. 5, Philadelphia, PA, Jan. 1982.

[19]Morrill, W., "ARAD Arc Tests," Missile and Space Div., Rept. PIR U-9361-189, General Electric Co., Philadelphia, PA, Aug. 1972.

[20]"Wiring Installation Assy, ARAD Sensors," Re-Entry Systems Operations, General Electric Co., Contract 08-737444-LD4, Drawing 47D523714, Rev. C, Feb. 1982.

[21]"Galileo Probe Operations Manual," Space and Communications Group, Hughes Aircraft Co., Rept. HS373-3726A, Nov. 1989.

[22]Metzger, J. W., "Measurements of Galileo Test ARAD Sensors," Re-Entry Systems Div., General Electric Co., Rept. PIR U-N8-82-9T20-048, Philadelphia, PA, Nov. 1982.

[23]"December 1992 Mission Sequence Test Report," Hughes Space and Communications Co., Rept. HS373-0020-3664, April 1993.

[24]Brewer, R. A., and Brant, D. N., "Thermal Protection System for the Galileo Mission Atmospheric Entry Probe," *Aerothermodynamics and Planetary Entry*, edited by A. L. Crosbie, Vol. 77, Progress in Astronautics and Aeronautics, AIAA, New York, 1981, pp. 309–334.

[25]Green, M. J., and Davy, W. C., "Galileo Probe Forebody Thermal Protection," AIAA Paper 81-1073, June 1981.

[26]Seiff, A., Venkatapathy, E., Haas, B. L., and Inteiri, P., "Galileo Probe Aerodynamics," AIAA Paper 96-2451, June 1996.

[27]Madara, S. E., "Analysis of Galileo Probe Aft Cover Heatshield Using Revised Base Heating for 335-kg Probe," Re-Entry Systems Div., General Electric Co., Rept. PIR U-N8-81-91-045, Philadelphia, PA, Sept. 1981.

[28]Howe, J. T., Pitts, W. C., and Lundell, J. H., "Survey of the Supporting Research and Technology for Thermal Protection of the Galileo Probe," *Thermophysics of Atmospheric Entry*, edited by T. E. Horton, Vol. 82, Progress in Astronautics and Aeronautics, AIAA, New York, 1982, pp. 293–327.

[29]Moss, J. N., "Advancements in Aerothermodynamics in Support of the Galileo Probe," *Proceedings of the Thirteenth International Symposium on Space Technology and Science*, AGNE, Tokyo, 1982, pp. 613–624.

[30]Kumar, A., and Graves, R. A., Jr., "User's Guide for the Computer Code 'COLTS' for Calculating the Coupled Laminar and Turbulent Flows Over a Jovian Probe," NASA TM 81848, June 1980.

[31]Brewer, R. A., Brant, D. N., and Fogaroli, R. P., "Development of a Steady-State Shape Change Ablation Code for the Design of Outer Planet Probes," AIAA Paper 77-95, Jan. 1977.

[32]Seiff, A., Kirk, B. D., Knight, T. C. D., Young, L. A., Milos, F. S., Venkatapathy, E., Mihalov, J. D., Blanchard, R. C., Young, R. E., and Schubert, G., "Thermal Structure of Jupiter's Upper Atmosphere Derived from the Galileo Probe," *Science*, Vol. 276, April 1997, pp. 102–104.

[33]Davies, C. B., and Park, C., "Trajectories of Solid Particles Spalled from a Carbonaceous Heat Shield," *Entry Vehicle Heating and Thermal Protection Systems: Space Shuttle, Solar Starprobe, Jupiter Galileo Probe*, edited by P. E. Bauer and H. E. Collicott, Vol. 85, Progress in Astronautics and Aeronautics, AIAA, New York, 1983, pp. 472–495.

[34]Lundell, J. H., "Spallation of the Galileo Probe Heat Shield," *Entry Vehicle Heating and Thermal Protection Systems: Space Shuttle, Solar Starprobe, Jupiter Galileo Probe*, edited by P. E. Bauer and H. E. Collicott, Vol. 85, Progress in Astronautics and Aeronautics, AIAA, New York, 1983, pp. 496–517.

[35]Haas, B. L., and Milos, F. S., "Simulated Rarified Entry of the Galileo Probe into the Jovian Atmosphere," *Journal of Spacecraft and Rockets*, Vol. 32, No. 3, 1995, pp. 398–403.

T. C. Lin
Associate Editor